3D Scan of Hardness Imprints for the Non-destructive In-Situ Structural Assessment of Operated Metal Components

Gabriella Bolzon[1] · **Marco Talassi**[1]

Abstract

The structural integrity of operated components can be assessed by non-destructive mechanical tests performed in-situ with portable instruments. Particularly promising in this context are small scale hardness tests supplemented by the mapping of the residual imprints left on metal surfaces. The data thus collected represent the input of inverse analysis procedures, which determine the material characteristics and their evolution over time. The reliability of these estimates depends on the accuracy of the geometry scans and on the robustness of the data filtering and interpretation methodologies. The objective of the present work is to evaluate the accuracy of the 3D reconstruction of the residual deformation produced on metals by hardness tests performed at a few hundred N load. The geometry data are acquired by portable optical microscopes with variable focal distance. The imperfections introduced by the imaging system, which may not be optimized for all ambient conditions when used in automatic mode, are analysed. Representative examples of the output produced by the scanning tool are examined, focusing attention on the experimental disturbances typical of onsite applications. Proper orthogonal decomposition and data reduction techniques are applied to the information returned by the instrumentation. The essential features of the collected datasets are extracted and the main noise is removed. The results of this investigation show that the accuracy achievable with the considered equipment and regularization procedures can support the development of reliable diagnostic analyses of metal components in existing structures and infrastructures.

1 Introduction

The structural integrity of operated components can be continuously monitored by non-destructive mechanical tests performed on site, with portable instruments. This approach can prevent the premature failure of large structures and infrastructures that are difficult to access, such as inshore and offshore windmills for the production of clean energy, and pipeline networks that transport hydrocarbons, hydrogen and water over long distances [1, 2]. These structural systems are mainly composed of welded portions of steel pipes, with effective mechanical properties that can vary over the time and space due to: chemical interactions; exposure to aggressive environments; the presence and the evolution of residual stresses; local heating developing at the welds and near the gas compression stations [3–9]. The related degradation processes can compromise the safety margins foreseen in design, while inhomogeneous distributions of the material properties can also be produced by the replacement of part of the operated components after accidental events like fire, explosions, impacts [10–13].

The local verification of the actual material properties may also be appropriate for other mechanical applications, including pressure vessels, manufacturing products and facilities, historical structures, joints and welds [14–20].

Damaging and aging processes in metals are mainly reflected by the evolution of the hardening response [3, 6, 21–25], which can be determined by instrumented indentation and hardness tests [26–51]. The high spatial resolution of these techniques permits to detect localized variations in material properties over time. These changes can play the role of early indicators of ongoing degradation phenomena.

Indentation tests can be performed onsite, directly on the operated component [32, 35, 50, 52] without any need to

✉ Gabriella Bolzon
  gabriella.bolzon@polimi.it

1   Department of Civil and Environmental Engineering, Politecnico di Milano, piazza Leonardo da Vinci 32, 20133 Milan, Italy

extract material samples and/or to machine specimens [41, 53, 54]. The most frequently acquired experimental information consists of the force applied to the indenter tip and of the corresponding penetration depth into the material [14, 19, 20, 27–32]. These pairs define the so-called indentation curves. The accuracy and reliability of the material properties deduced from these data can be improved by the consideration of the residual deformation left on metal surfaces, following a methodology that is rapidly spreading in different contexts [33–43].

Eventually, geometry data alone can be exploited for diagnostic purposes [34, 49]. In fact, the permanent deformation produced by hardness test on structural metals reflects the main constitutive properties that govern the plastic flow, such as the yield limit and the material strength [3, 6, 10, 23]. The value of these parameters can be extracted from geometry measurements using inverse analysis procedures that combine the experimental output with a validated simulation model of the test. Thus, each set of constitutive properties can be associated to an indentation profile.

Indentation and hardness tests can be carried out at different load levels. Values typical of structural applications (1-2 kN) are for instance considered in [35, 37, 55]. Forces lower by one order of magnitude, consistent with superficial investigations according to ASTM E18 Standards classification [56], are applied in [32, 43, 49].

Reducing the load facilitates onsite applications as both the equipment encumbrance and the image acquisition time are reduced. Portable durometers and compact scanners, at present widely available on the market, can be mounted on the arms of collaborative robots powered by solar cells, and/or on frames that move on rails. The measurements can be transferred through virtual networks, and processed to return the sought material characteristics in near real time [36, 37, 57, 58]. Thus, fully automated testing campaigns can be planned, overcoming the difficulties associated to the large extensions and difficult accessibility of some strategic infrastructures.

Experimental data collected on site are usually affected by various disturbances, which may compromise the reliability of the mechanical predictions. The imperfections associated to the geometry scans, depending also on the measured dimensions, and their source are the subject of the present investigation. Data interpretation and filtering procedures are also introduced in this contribution, which aims to provide useful suggestions for practical applications.

The measurement system considered in this work is based on focus-variation light microscopy, widely used to perform micro-topography measurements and evaluate the quality of surfaces and industrial products; see, e.g. [44–48]. The instrumentation combines optics with a limited depth of field with a vertical movement of the scanning tool. The signal is processed to identify the focused part of the acquired images. These portions are then combined in order to reconstruct a detailed three-dimensional (3D) view. The final result can be returned in digital format and further processed and displayed, e.g. in the form of geometry maps or profiles.

The objective of the present investigation is to evaluate the accuracy of the mapping of the residual deformation produced on metals by hardness tests performed at a few hundred N load. The imperfections introduced by the imaging system, which may not be optimized for all ambient conditions when used in automatic mode, are analysed.

Proper orthogonal decomposition and data reduction techniques are applied to the information returned by the instrumentation. The essential features of the collected datasets are extracted, and the main experimental disturbances are removed.

The results of this work show that the accuracy achievable with the considered equipment and regularization methodologies can support the development of reliable material calibration procedures for the diagnostic analysis of metal components in existing structures and infrastructures.

The presentation is organized as follows. The material characterization procedures based on the imprint mapping are introduced first, in Sect. 2.1. The experimental information provided by the optical devices considered in this work is illustrated in Sect. 2.2, while the main results of former investigations in the envisaged context are summarized in Sect. 2.3. The imperfections that can affect the geometry scan are considered next, in Sect. 3, focusing attention on the output of optical microscopes with variable focal distance. The relevance for the diagnostic analysis of the experimental disturbances is evaluated in Sect. 3.1, while regularization procedures are proposed in Sect. 3.2.

2 Material Characterization by Imprint Mapping

The permanent deformation produced by hardness tests reflects the mechanical characteristics of metals in indirect manner. Thus, the main constitutive parameters can be identified by inverse analysis procedures, which entail the comparison between the experimental output and the corresponding results of an accurate simulation model of the test. Non-linear finite element methods (FEMs) are often used to this purpose, e.g. [35, 36, 39, 43, 54]. Alternatively, equivalent analytical surrogates that operate in near real time are introduced [57].

Inverse analysis rests on the iterative updating of the constitutive properties, given as input in the simulation tool, until the discrepancy between the experimental results and the calculated ones is minimized. The optimum set of constitutive values is then assumed to coincide with the actual material characteristics. The overall procedure is schematized in Fig. 1.
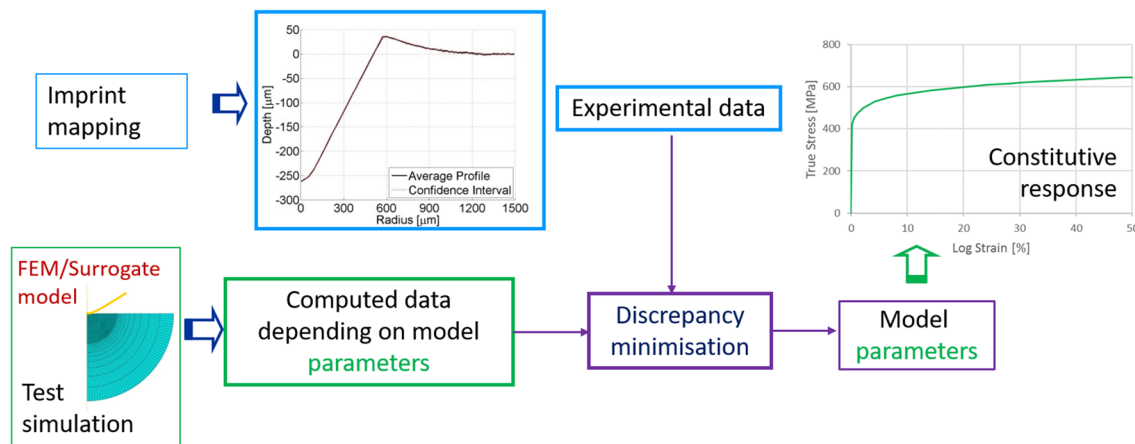
Fig. 1 Schematic of the inverse analysis procedure

2.1 Simulation Models

The metal response to indentation can be reproduced by traditional elastic-plastic constitutive laws, where Young's modulus E and Poisson's ratio ν characterize the initial reversible behaviour. These properties can be assumed constant during the lifetime of most structures.

Beyond elasticity, the classical Hencky–Huber–von Mises (HHM) plasticity model is often selected, and the exponential hardening rule is introduced:

$$\sigma\left(\varepsilon^p\right) = \sigma_y\left(1 + \frac{E\varepsilon^p}{\sigma_y}\right)^n. \tag{1}$$

In relation (1), the scalar variables σ and ε^p represent the equivalent (in HHM sense) true (Cauchy) stress and the plastic component of the logarithmic strains, respectively, while the initial yield limit σ_y and the exponent n are the main material parameters to be identified for the diagnosis of operated components.

The constitutive response in terms of nominal (engineering) values [59], typical of traditional tensile tests, and the material strength can then be recovered by applying the incompressibility constraint to the irreversible strains.

The yield limit and strength are affected by material aging and other damaging phenomena. These parameters are also reflected by the results of indentation and hardness tests, which can be reproduced by combining the constitutive relations with finite element discretization [34, 35, 49]. Equivalent analytical surrogates may then be introduced to reduce the computational burden. In any case, the accuracy of the simulation models is independent of the applied load, and can rely on previous validation work [34–43].

2.2 Experimental Information

The permanent deformation produced by indentation on metal surfaces can be mapped by several portable devices. Optical microscopes with variable focal distance (Alicona IF system) are considered in this study [44, 60].

The portable equipment used in the present investigation is shown in Fig. 2b visualizes the micrograph of an indented metal surface while the snapshot in Fig. 2c displays the 3D reconstruction of the residual deformation, as reproduced by the software supplied with the instrument.

The microscope mounts 4 optics ($2.5\times$, $5\times$, $10\times$, $20\times$), and allows to investigate the morphology of different surfaces over a wide depth range, with a vertical resolution up to 50 nm. Vision can be improved by optimizing the lighting conditions, automatically setting or manually adjusting brightness and contrast.

Dedicated software is installed on a computer connected to the instrument. It controls the focus variations and the movements (up to 130 mm in the vertical direction, 95 mm horizontally) required for the sequential imaging of large areas.

The acquired information can be viewed as shown in Fig. 2, and stored in digital format. The data can be further processed and represented in various ways, as for example displayed in Figs. 3 and 4, and in the following graphs.

Figure 3a visualizes the geometry of the imprint generated by an axisymmetric Rockwell tip [55, 56] pressed against the surface of a pipeline steel at 2 kN maximum load [35]. Since the material is isotropic, the imprint is axisymmetric and fully represented by the mean curve displayed in Fig. 3b

The profile and confidence limits reported in Fig. 3b are obtained from the coordinates describing eight radial cross sections of the 3D graph in Fig. 3a, equally rotated (by 45 degrees) with respect to each other. The confidence interval is barely visible as the measurement dispersion is extremely
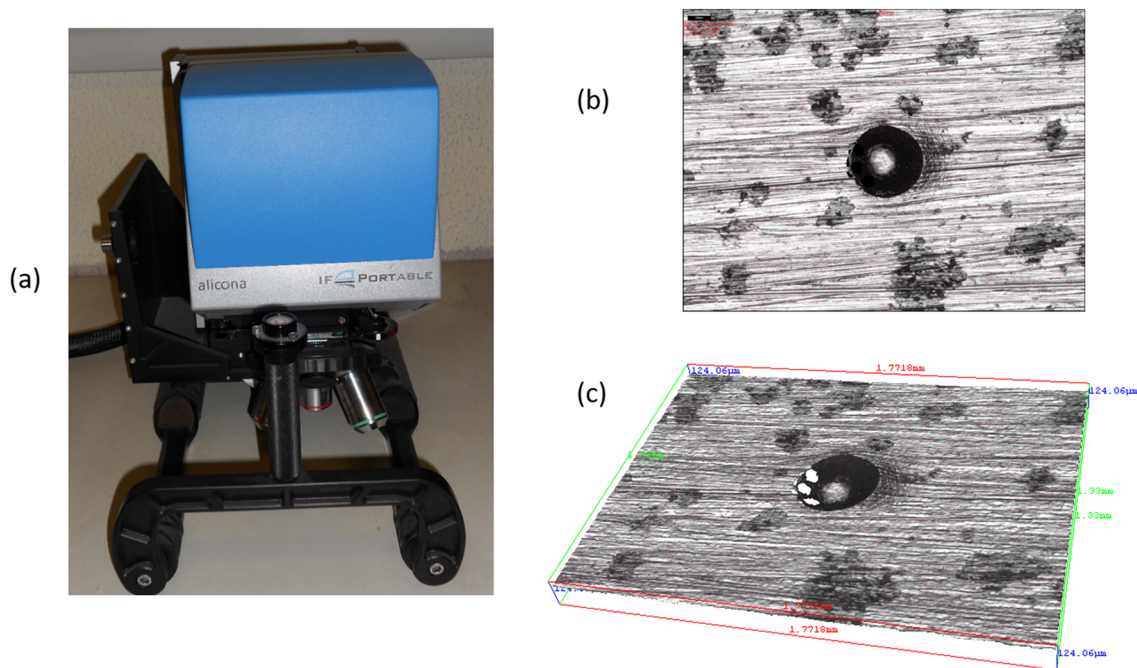
Fig. 2 The portable optical microscope with variable focal distance used in the present study (**a**); the micrograph (**b**) and the 3D reconstruction (**c**) of an indented metal surface
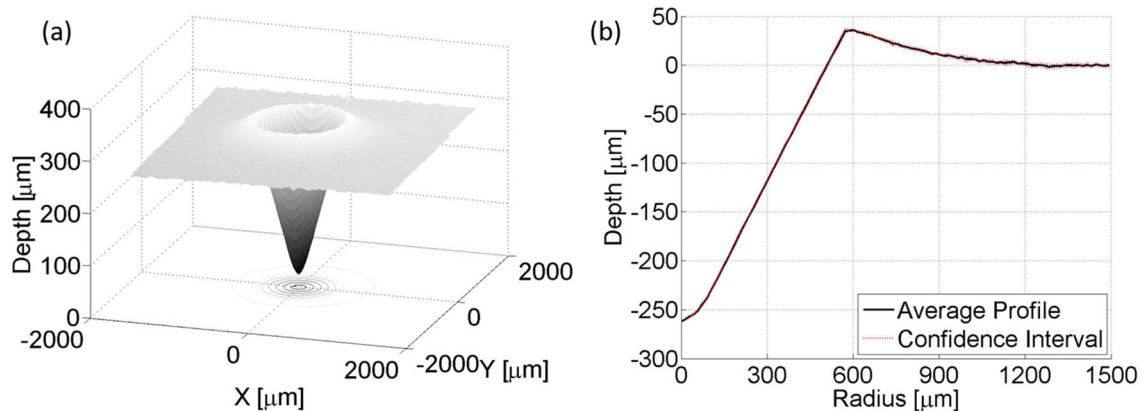

Fig. 3 Geometry of the residual deformation generated by Rockwell indentation: **a** 3D mapping of the imprint produced at 2 kN load on pipeline steel; **b** mean profile and confidence limits

low also thanks to the accuracy of the scan, in this case performed in lab.

Applied forces of an order of magnitude lower than that producing the output shown in Fig. 3 have also been considered for material characterization purposes [32, 43, 49].

Figure 4 compares the contour plot of the residual deformation left on pipeline steel by hardness tests carried out at 2 kN and 0.2 kN load. The area of the square domain represented in Fig. 4a is 4 times larger than the one in Fig. 4b. Thus, the imprint produced by 0.2 kN force can be mapped in one shot, within seconds. In contrast, the representation of the residual deformation corresponding to 2 kN load requires image stitching, and a few minutes to process the data. The

different run time is especially significant when the scan is performed in situ on operated components, and repeated hundreds of times.

2.3 Former Identification Results

The coordinates representing the mean profile of an indented metal surface can be obtained as described in Sect. 2.2. These data can be supplied to the inverse analysis procedure schematically outlined in Fig. 1, to identify the main mechanical properties of the material [35].

Figure 5 compares the experimental curve represented in Fig. 3b with the output of the simulated indentation test,
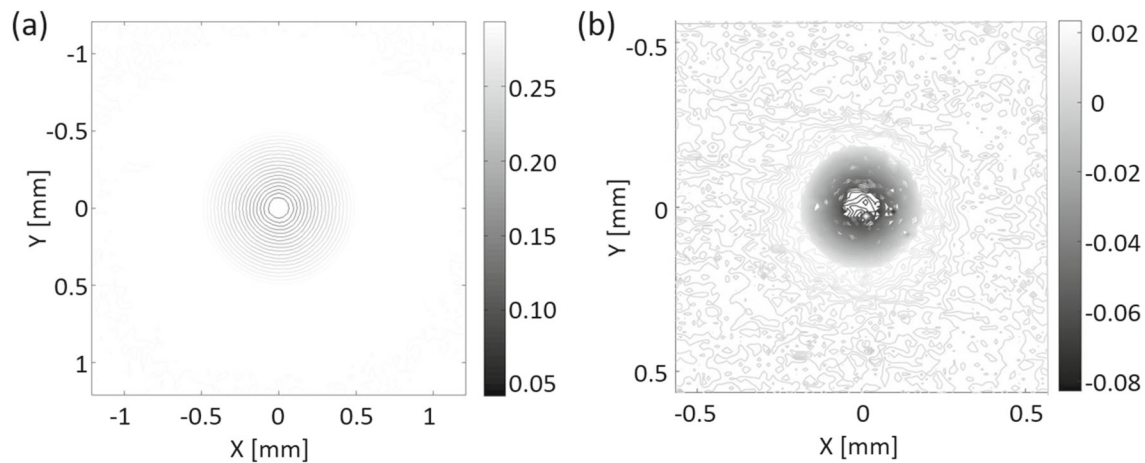
Fig. 4 Contour plot of the residual deformation produced on pipeline steel by hardness tests for the applied load: **a** 2 kN; **b** 0.2 kN
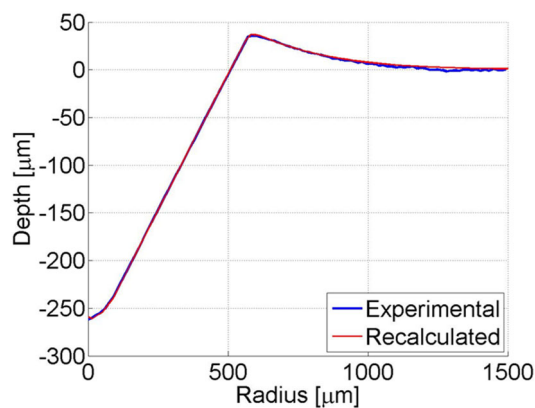

Fig. 5 Comparison between the experimental imprint geometry of Fig. 3b and the output of the numerical simulation performed with the identified material parameter set [35]
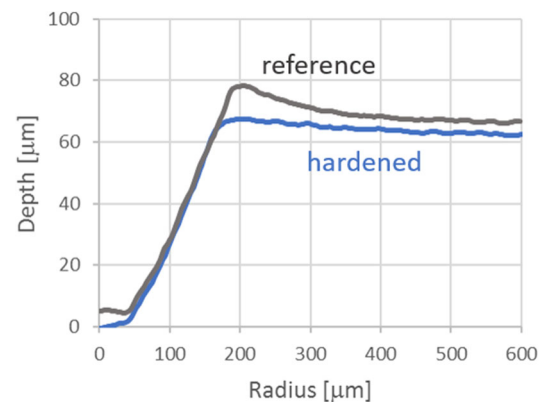

Fig. 6 Comparison between the indentation response of X70 steel in reference and mechanically hardened conditions (Rockwell tip, 0.2 kN load) [49]

using the identified values of the parameters σ_y and n (1) as input data. The good correspondence between the experimental profile and the recalculated geometry is due both to the accuracy of the numerical model and to the reliability of the inverse analysis procedure.

The simulation model can also be used to quantify the influence of the metal properties on the residual deformation produced by indentation [61]. Sensitivity analyses show that the parameters governing the plastic flow (in particular, the yield limit and strength) are particularly reflected by the piling up region surrounding the sinking material. Conversely, the imprint portion below the reference plane mainly reproduces the geometry of the penetrating tip. This feature is clearly visible in Figs. 3b and 5, which display the 120° opening angle and the rounded end with 200 μm radius of the sphero-conical Rockwell tip [55, 56].

The imprint profiles shown in Figs. 6 and 7 are obtained from data sets similar to that visualized in Fig. 4b. The curves in Fig. 6 compare the indentation response of X70 pipeline

Fig. 7 Comparison between the indentation response of 17H1S steel in as received status and after 36 and 51 operation years (Rockwell tip, 0.2 kN load) [49]

steel in reference conditions, and after mechanically induced hardening. The graphs of Fig. 7 show the evolution, with operation time, of the irreversible deformation produced by a Rockwell tip on 17H1S steel at 0.2 kN load.

Table 1 Mechanical properties of 17H1S steel determined from imprint mapping and tensile test

	Imprint mapping [49]		Tensile test [25]	
	Yield limit [MPa]	Strength [MPa]	Yield limit [MPa]	Strength [MPa]
As received	390	524	357	547
Aged, 36 years	351	576	405	563
Aged, 51 years	416	730	449	610

Table 1 lists the main mechanical properties obtained from the curves drawn in Fig. 7, applying the procedure outlined in Fig. 1, and from traditional uniaxial tests. The agreement is quite good despite the different material volumes involved in indentation and traction tests [49].

3 3D Scan of Hardness Imprint

The results of the previous studies, summarized in Sect. 2, show the potential of non-destructive diagnostic analyses based on hardness tests performed on operated components at a few hundred N load. The considered methodology is based on the mapping of the residual deformation left on the investigated metal surfaces. Optical microscopes with variable focal distance are used [44].

The geometry scans obtained with the instrument presented in Sect. 2.2 (optics 10×; vertical and horizontal resolution: 1 and 7.5 μm, respectively) are further analysed in this section. The 3D coordinates of 4000 points lying on the explored surfaces are considered. These data are processed in Matlab environment [62].

The graphs shown in Fig. 8 represent the profile of three imprints (nominally identical) produced by a Rockwell tip pressed against the surface of X70 steel at 200 N load. Figure 8a refers to the initial material status, Fig. 8b concerns mechanically hardened conditions. The curves associated with each situation are quite repetitive, confirming the representativeness of each mapping [49]. Their average is displayed in Fig. 6.

The dimensions of the mapped regions allow to highlight the roughness of the indented surface, barely visible in the profiles of Fig. 3 obtained at 2 kN load. On the other hand, the rounded end of the Rockwell tip is well defined in Figs. 3 and 5, not so in Fig. 8.

The arrow in Fig. 8a points out a major deviation from the expected trend. This anomaly is due to the deposition of dust particles difficult to remove since, in this case, the mapping was performed several days after the indentation test.

Other disturbances can be related to the features of the imaging system, which may not be optimized for all ambient conditions when used onsite, with automatic setting. Examples are given in Fig. 9, which graphically represents the raw data returned by the equipment employed in the present study. The mapping has been performed under different lighting conditions.

Figure 10 displays eight radial cross sections and the mean profiles extracted from the 3D datasets visualized in Fig. 9. Micrographs of the indented surfaces are also shown. The corresponding imprints are labelled A and B.

Case A shows peaks of light reflected from the bottom of the imprint, which acts as a mirror. In contrast, when the light intensity is reduced, some information may also be lost in the piling up region of the mapped surface (case B). The missing data are replaced by the linear interpolation of the available ones [62]. However, the geometry reconstruction may be distorted around the sunken area of imprint B.

The informative content of the geometries visualized in Figs. 9 and 10 can be evaluated by proper orthogonal decomposition (POD) [63]. This procedure allows to represent the data in an orthonormal reference system different from the Cartesian one. In the present context, the POD bases correspond to primary deformation modes.

3.1 POD Representation

In this study, the POD representation of the imprints considers the 8 radial cross sections extracted from the 3D scans following the procedure outlined in Sect. 2.2. The corresponding Cartesian coordinates are stored in the 8 columns of matrix U.

The POD bases are defined by the eigenpairs (eigenvectors V_i and eigenvalues λ_i, $i = 1, \ldots 8$) of the square matrix $D = U^T U$. Each basis is represented by the vector $\boldsymbol{\Phi}_i$, such that:

$$\boldsymbol{\Phi}_i = \frac{1}{\sqrt{\lambda_i}} U V_i, \tag{2}$$

where λ_i plays a normalization role.

The original information stored in matrix U can then be reconstructed from the linear combination of the bases $\boldsymbol{\Phi}_i$ and the amplification factors defined by the row vectors $A_i = \boldsymbol{\Phi}_i^T U$.

As a typical POD feature, the decay rate of the eigenvalue sequence (see, for example, Table 2) can be associated with the information content of the original data, projected onto
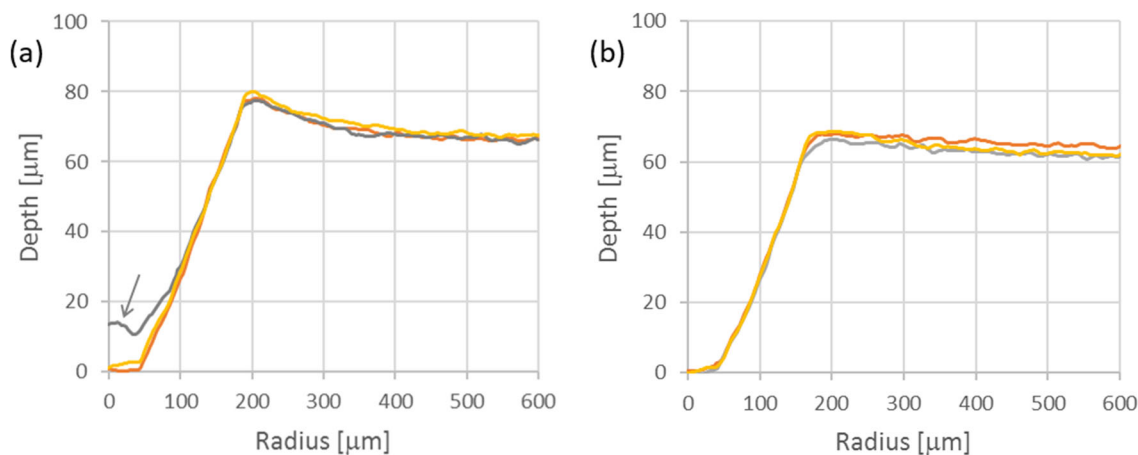
Fig. 8 Half mean profiles of the imprints produced by an axisymmetric Rockwell tip on pipeline steel: **a** initial material status; **b** hardened conditions
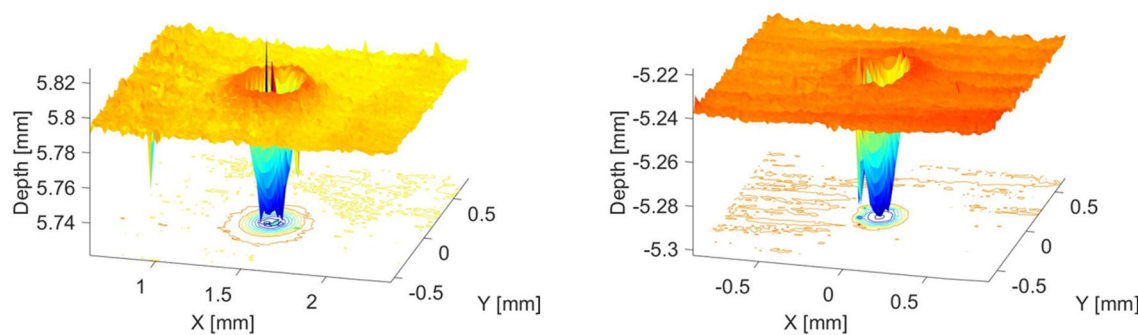

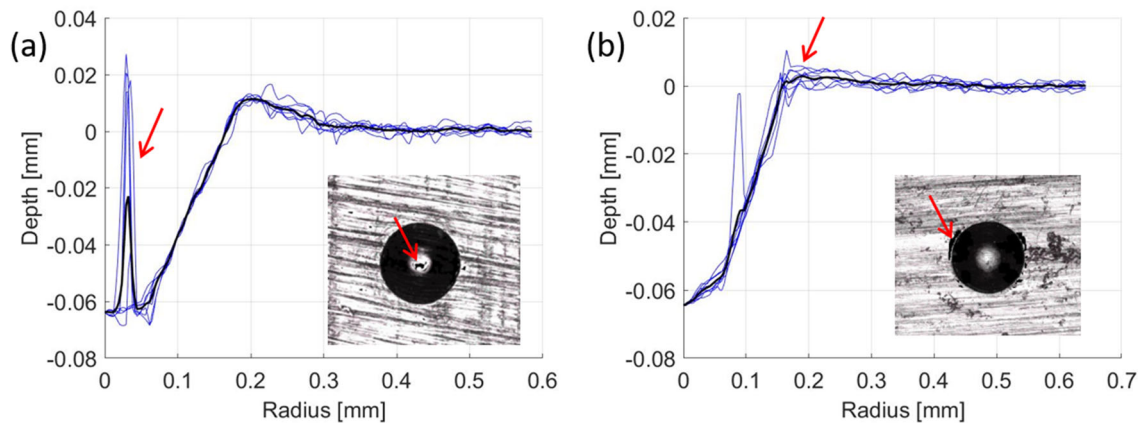**Fig. 9** Graphical representation of raw datasets returned by the equipment shown in Fig. 2

Fig. 10 Blue lines: radial cross sections of the imprints A (**a**) and B (**b**); black curve: mean profile. Micrographs of the indented metal surfaces in the inserts (Color figure online)

Table 2 Eigenvalues associated to the POD of the profiles visualized in Fig. 10

	1st	2nd	3rd	4th
Imprint A	0.9270	0.0352	0.0065	0.0021
Imprint B	0.8252	0.0050	0.0014	0.0011
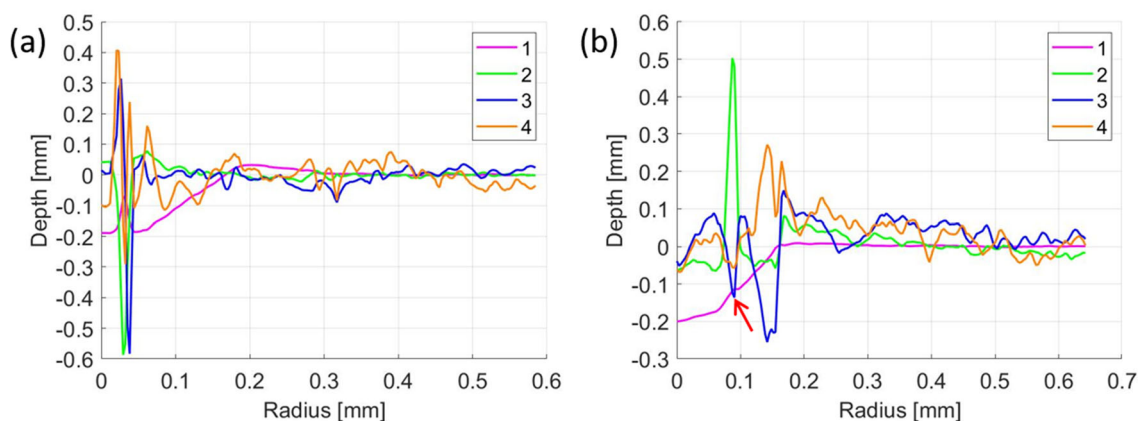
Fig. 11 The first four POD bases associated to the profiles extracted from the imprints A (**a**) and B (**b**), visualized in Fig. 10
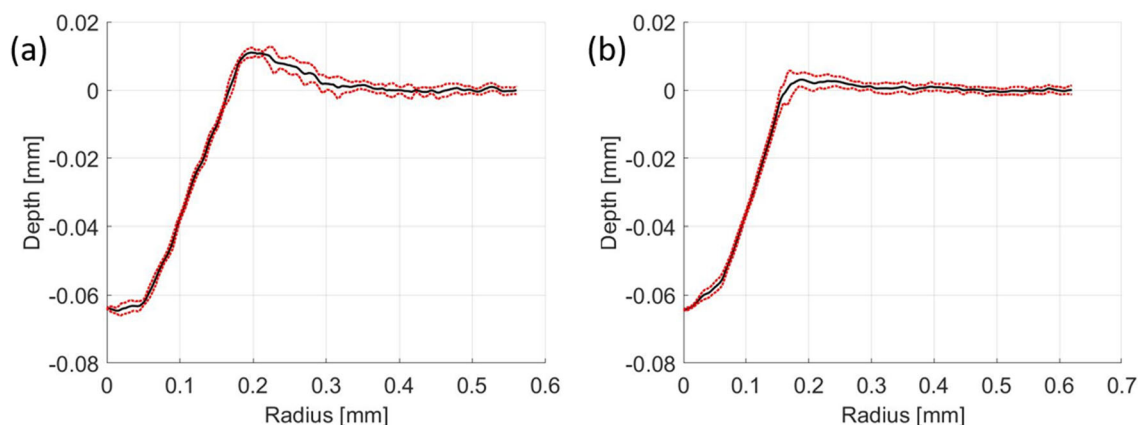

Fig. 12 Mean profile (black continuous line) and confidence limits (red dashed lines) of the imprints A (**a**) and B (**b**), filtered data (Color figure online)

each basis (here, as anticipated, primary deformation mode) [63].

The first four bases of the POD representation of imprints A and B are shown in Fig. 11.

Mode 1 (pink line) consists of the scaled mean profile of the permanent deformation left on the metal surface. In case A, this curve is affected by the systematic presence of the light peaks reflected from the bottom of the imprint. In case B, the curve presents a small deviation from the expected trend at about 0.1 mm from the symmetry axis. This anomaly is due to the reflection peak affecting one cross section in Fig. 10b.

The other bases contain noises. In case B, Fig. 11b, all modes except the first, show pronounced variations in the zone between the free surface and the sunken region.

The most frequent anomalies are located below the original level of the indented plane. These data show a low sensitivity to the material characteristics and, therefore, do not influence significantly the identification of the constitutive properties [49]. In fact, see Sect. 2, the lower part of the

imprint profile mainly reproduces the geometry of the indenter tip. This feature can be exploited to filter the experimental disturbances.

In the sunken region, the imprint geometry can be regularized by neglecting the scan points located outside a band of pre-defined width (say, δ) from the ideal Rockwell profile [49]. Figure 12 shows the results of this procedure for $\delta \pm 2.5$ μm.

The graphs in Fig. 13 compare the mean curves of Fig. 12 with those of Fig. 10. Major deviations from the expected trend are removed and the plots overlap largely.

3.2 Lacking Data

Under some lighting conditions, the equipment cannot acquire the entire area of interest. This is the case of imprint B.

The missing information is highlighted in Fig. 14, which displays the raw measurements provided by the optical device in a different way, namely: the sets of out-of-plane coordinates placed on the upper third, middle third and lower third
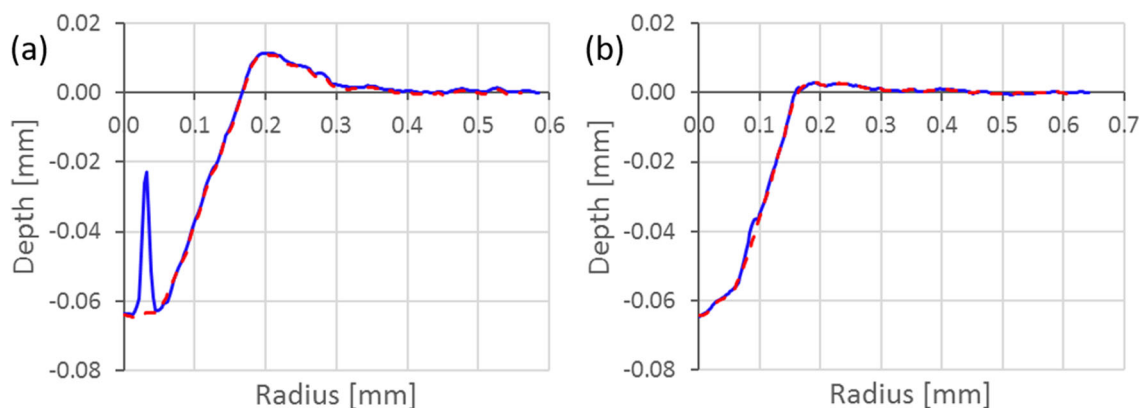
Fig. 13 Comparison between the mean profiles represented in Fig. 10 (blue continuous lines) and Fig. 12 (red dashed lines): imprint A (**a**) and B (**b**) (Color figure online)
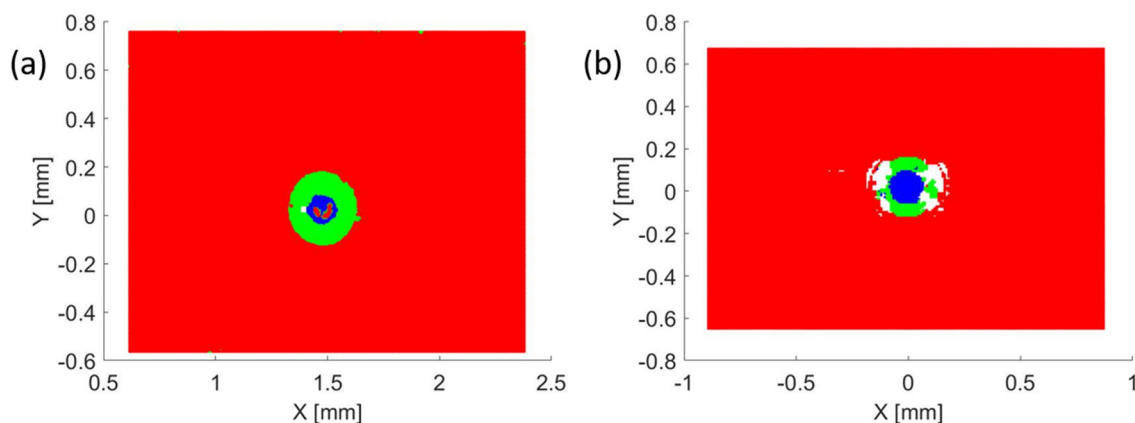

Fig. 14 Color map of the distribution of the measured out-of-plane coordinates of the imprints A (**a**) and B (**b**); red: upper third; green: middle third; blue: lower third; white: missing data (Color figure online)

of the imprint depth define the red, green and blue regions, respectively; white areas correspond to lacking data.

The missing data are usually replaced by the linear interpolation of the available ones [62], but this procedure could affect the geometry reconstruction. This eventuality is verified here by considering 6 alternative cross sections of imprint B, manually extracted from the more densely populated areas of Fig. 14b. These profiles are represented in Fig. 15a with the corresponding mean curve.

Figure 15b shows the mean curve of Fig. 15a compared with the profile resulting from the automatic selection of the cross sections, see Fig. 10. The difference is almost negligible.

As a further verification exercise, some coordinate sets are artificially removed from the imaging data of imprint A, which presents a marked piling-up. The main peaks of reflected light are also eliminated in this application.

The raw distribution of the retained information, represented in Fig. 16a, mimics that in Fig. 14a. Figure 16b shows the 3D reconstruction of the altered scan, with the empty

areas replaced by the linear interpolation of the available coordinates [62].

The profiles displayed in Fig. 17a are extracted automatically from the dataset represented in Fig. 16b. The corresponding average curve, represented in Fig. 17b, is almost superimposed on the original one shown in Fig. 12a.

4 Conclusion

The present work considers a wide spreading approach to the mechanical characterization of metals based on indentation and hardness tests. The experimental campaign can be performed in situ, applying relatively low forces to reduce encumbrance and improve maneuverability of portable equipment.

The study focuses on the contribution made by the mapping of the residual imprint to the calibration of the mechanical parameters that reflect the degradation processes taking place in the material.
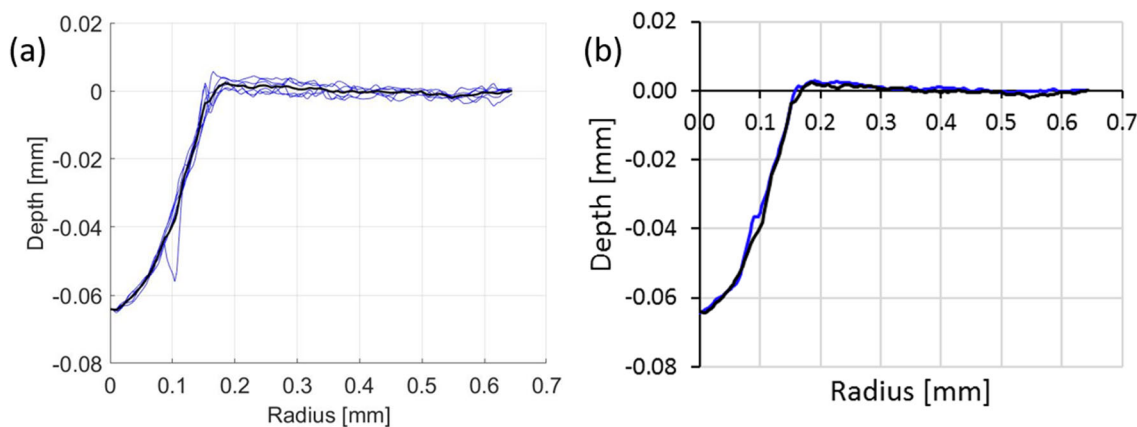
Fig. 15 a Manually selected cross sections of imprint B (thin blue lines) and corresponding mean curve (black); **b** comparison between the mean profile in graph (a) and in Fig. 10b: black and blue line, respectively (Color figure online)
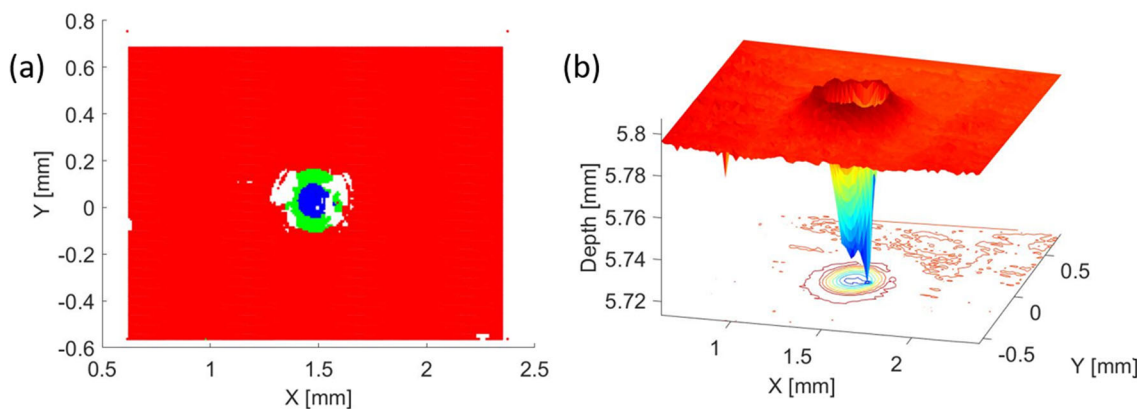

Fig. 16 a Color map of the out-of-plane distribution of the retained coordinates of imprint A: white areas denote missing data; **b** 3D reconstruction of the altered scan
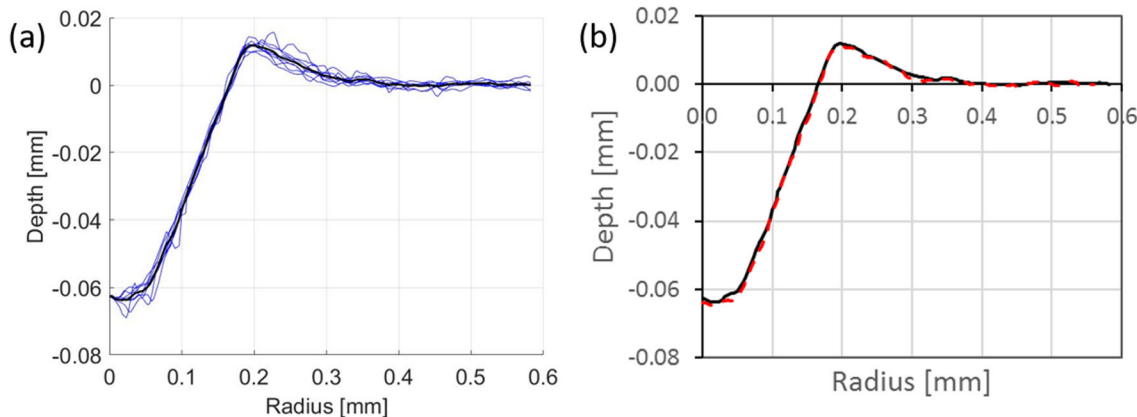

Fig. 17 a Profiles extracted from the 3D map represented in Fig. 16b (thin blue lines), and the corresponding mean curve (black); **b** the mean curve **a** and the original one of Fig. 12a (red dashed curve) (Color figure online)

The considered operative procedure combines two main ingredients:

– the experimental data, affected by almost inevitable perturbations that depend on the test size, the execution mode and the main characteristics of the mapping tools;
– a realistic simulation model of the experiment, free of the above limitations.

The considered measurements are performed by optical microscopes with variable focal distance. Attention is paid to the inaccuracies associated with the imaging system, which may not be optimized for all ambient conditions when used onsite, in automatic mode. In fact, the accuracy of the geometry scans significantly affects the reliability of the safety predictions.

Simple regularization procedures are proposed to overcome the major experimental disturbances, which are emphasized by the small size of the mapped imprints. The suggested methodology allows to reliably support the diagnostic analysis of even large structures located in harsh environment. Safe lifetime can thus be extended and operation costs reduced through timely repair plans and retrofit interventions on damaging components.

Author Contributions GB: conceptualization; experimental investigation; manuscript draft and revision; figures. MT: numerical investigation; manuscript revision; preliminary graphs.

Data Availability The datasets analysed during the current study are available from the corresponding author on reasonable request.

Declarations

Conflict of interest The authors declare no competing interests.

Ethical Approval Not applicable.

Consent to Participant Not applicable.

Consent for Publication Not applicable.

References

1. Sherif, S.A., Barbir, F., Veziroglu, T.N.: Wind energy and the hydrogen economy—review of the technology. Sol. Energy **78**, 647–660 (2005). https://doi.org/10.1016/j.solener.2005.01.002
2. Haesen, E., Vingerhoets, P., Koper, M., Georgiev, I., Glenting, C., Goes, M., Hussy, C.: Investment needs in trans-European energy infrastructure up to 2030 and beyond. Final Report. Publications Office of the European Union, Luxembourg (2018)
3. Nykyforchyn, H., Lunarska, E., Tsyrulnyk, O.T., Nikiforov, K., Gennaro, M.E., Gabetta, G.: Environmentally assisted in-bulk steel degradation of long term service gas trunkline. Eng. Fail. Anal. **17**, 624–632 (2010). https://doi.org/10.1016/j.engfailanal.2009.04.007
4. Ren, L., Jiang, T., Jia, Z., Li, D., Yuan, C., Li, H.: Pipeline corrosion and leakage monitoring based on the distributed optical fiber sensing technology. Measurement. **122**, 57–65 (2018). https://doi.org/10.1016/j.measurement.2018.03.018
5. Wright, R.F., Lu, P., Devkota, J., Lu, F., Ziomek-Moroz, M., Ohodnicki, P.R., Jr.: Corrosion sensors for structural health monitoring of oil and natural gas infrastructure: a review. Sensors **19**, 3964 (2019). https://doi.org/10.3390/s19183964
6. Bolzon, G., Gabetta, G., Nykyforchyn, H.: Degradation Assessment and Failure Prevention of Pipeline Systems. Lecture Notes in Civil Engineering. Springer, Berlin (2020)
7. Kumar, S., Pandey, C., Goyal, A.: A microstructural and mechanical behavior study of heterogeneous P91 welded joint. Int. J. Pres. Ves Pip. **185**, 104128 (2020). https://doi.org/10.1016/j.ijpvp.2020.104128
8. Farzadi, A.: Gas pipeline failure caused by in-service welding. J. Pres. Ves Tech. **138**, 011405 (2016). https://doi.org/10.1115/1.4031443
9. Mirzaee-Sisan, A.: Welding residual stresses in a strip of a pipe. Int. J. Pres. Ves Pip. **159**, 28–34 (2018). https://doi.org/10.1016/j.ijpvp.2017.11.007
10. Moan, T.: Life cycle structural integrity management of offshore structures. Struct. Infrastr Eng. **14**, 911–927 (2018). https://doi.org/10.1080/15732479.2018.1438478
11. Chou, J.-S., Tu, W.-T.: Failure analysis and risk management of a collapsed large wind turbine tower. Eng. Fail. An. **18**, 295–313 (2011). https://doi.org/10.1016/j.engfailanal.2010.09.008
12. Alonso-Martinez, M., Adam, J.M., Alvarez-Rabanal, F.P., del Coz Díaz, J.J.: Wind turbine tower collapse due to flange failure: FEM and DOE analyses. Eng. Fail. An. **104**, 932–949 (2019). https://doi.org/10.1016/j.engfailanal.2019.06.045
13. Chu, Q., Zhang, M., Li, J., Chen, Y., Luo, H., Wang, Q.: Failure analysis of a steam pipe weld used in power generation plant. Eng. Fail. Anal. **44**, 363–370 (2014). https://doi.org/10.1016/j.engfailanal.2014.05.019
14. Byun, T.S., Hong, J.H., Haggag, F.M., Farrell, K., Lee, E.H.: Measurement of through-the-thickness variations of mechanical properties in SA508 Gr.3 pressure vessel steels using ball indentation test technique. Int. J. Pres. Ves Pip. **74**(3), 231–238 (1997). https://doi.org/10.1016/S0308-0161(97)00114-2
15. Lewandowski, J.J., Seifi, M.: Metal additive manufacturing: a review of mechanical properties. Annu. Rev. Mater. Res. **46**(1), 151–186 (2016). https://doi.org/10.1146/annurev-matsci-070115-032024
16. Mark, D., Bowman, A.M., Piskorowski: Evaluation and repair of wrought iron and steel structures in Indiana. Technical

Report FHWA/IN/JTRP-2004/4, SPR-2655, Purdue University West Lafayette, IN (2004)

17. Kowal, M., Mirosław Szala, M.: Diagnosis of the microstructural and mechanical properties of over century-old steel railway bridge components. Eng. Fail. Anal. **110**(104447), 1–17 (2020). https://doi.org/10.1016/j.engfailanal.2020.104447

18. Kaur, A., Ribton, C., Balachandaran, W.: Electron beam characterisation methods and devices for welding equipment. J. Mater. Process. Technol. **221**, 225–232 (2015). https://doi.org/10.1016/j.jmatprotec.2015.02.024

19. Arai, M., Takahashi, Y., Kumagai, T.: Determination of high temperature elastoplastic properties of welded joints by indentation test. Mater. High. Temp. **32**(5), 475–482 (2015). https://doi.org/10.1179/0960340915Z.000000000123

20. Du, Z., Kuilong Xu, K., Wang, L., Zhang, X., Zhang, X.: Characterization of the local mechanical properties of 5083–5383 MIG welded joints. J. Phys.: Conf. Ser. **2390**(012013), 1–8 (2023). https://doi.org/10.1088/1742-6596/2390/1/012013

21. National Research Council: Accelerated Aging of Materials and Structures: the Effects of Long-Term Elevated-Temperature Exposure. The National Academies Press, Washington DC (1996). https://doi.org/10.17226/9251

22. Gür, C.H., Yildiz, I.: Utilization of non-destructive methods for determining the effect of age-hardening on impact toughness of 2024 Al–Cu–Mg alloy. J. Nondestruct Eval. **27**, 99–104 (2008). https://doi.org/10.1007/s10921-008-0028-2

23. Maruschak, P.O., Salo, U.V., Bishchak, R.T., Poberezhnyi, L.Y.: Study of main gas pipeline steel strain hardening after prolonged operation. Chem. Petr Eng. **50**, 58–61 (2014). https://doi.org/10.1007/s10556-014-9855-4

24. Velicheti, D., Nagy, P.B., Hassan, W.: Stress assessment in precipitation hardened IN718 nickel-base superalloy based on Hall coefficient measurements. J. Nondestruct Eval. **36**, 13 (2017). https://doi.org/10.1007/s10921-017-0393-9

25. Nykyforchyn, H.: In-service Degradation of Pipeline Steels. Lecture Notes in Civil Engineering. Springer, Berlin (2020). https://doi.org/10.1007/978-3-030-58073-5_2

26. Bolzon, G.: Non-destructive Mechanical Testing of Pipelines. Lecture Notes in Civil Engineering. Springer, Berlin (2020). https://doi.org/10.1007/978-3-030-58073-5_1

27. ISO 14577:2002:. Metallic materials—instrumented indentation test for hardness and materials parameters

28. ISO/TR Standards 29381 Metallic materials—measurement of mechanical properties by an instrumented indentation test-indentation tensile properties

29. Tariq, F., Naz, N., Baloch, R.A., Faisal: Characterization of material properties of 2xxx Series Al-alloys by non destructive testing techniques. J. Nondestruct Eval. **31**, 17–33 (2012). https://doi.org/10.1007/s10921-011-0117-5

30. Midawi, A.R.H., Simha, C.H.M., Gerlich, A.P.: Assessment of yield strength mismatch in X80 pipeline steel welds using instrumented indentation. Int. J. Pres. Ves Pip. **168**, 258–268 (2018). https://doi.org/10.1007/s13632-020-00693-8

31. Wang, Z., Deng, L., Zhao, J.: Estimation of residual stress of metal material without plastic plateau by using continuous spherical indentation. Int. J. Pres. Ves Pip. **172**, 373–378 (2019). https://doi.org/10.1016/j.ijpvp.2019.04.008

32. Chen, G., Zhong, J., Zhang, X., Guan, K., Wang, Q., Shi, J.: Estimation of tensile strengths of metals using spherical indentation test and database. Int. J. Pres. Ves Pip. **189**, 104284 (2021). https://doi.org/10.1016/j.ijpvp.2020.104284

33. Mulford, R., Asaro, R.J., Sebring, R.J.: Spherical indentation of ductile power law materials. J. Mater. Res. **19**, 2641–2649 (2004). https://doi.org/10.1557/JMR.2004.0363

34. Bolzon, G., Buljak, V., Maier, G., Miller, B.: Assessment of elastic-plastic material parameters comparatively by three procedures based on indentation tests and inverse analysis. Inv Probl. Sci. Eng. **19**(6), 815–837 (2011). https://doi.org/10.1080/17415977.2011.551931

35. Bolzon, G., Molinas, B., Talassi, M.: Mechanical characterisation of metals by indentation tests: An experimental verification study for on-site applications. Strain. **48**(6), 517–527 (2012). https://doi.org/10.1111/j.1475-1305.2012.00850.x

36. Bolzon, G.: Advances in experimental mechanics by the synergetic combination of full-field measurement techniques and computational tools. Measurement. **54**, 159–165 (2014). https://doi.org/10.1016/j.measurement.2014.04.020

37. Bolzon, G., Gabetta, G., Molinas, B.: Integrity assessment of pipeline systems by an enhanced indentation technique. ASCE J. Pipeline Syst. Eng. Practice **6**(1), 04014010 (2015). https://doi.org/10.1061/(ASCE)PS.1949-1204.0000183

38. Pöhl, F., Schwarz, S., Junker, P., Hackl, K., Theisen, W.: Indentation and scratch testing-experiment and simulation. Int. Conf. Stone Concrete Mach. (ICSCM) **3**, 292–308 (2015). https://doi.org/10.13154/icscm.3.2015.292-308

39. Wang, M., Wu, J., Hui, Y., Zhang, Z., Zhan, X., Guo, R.: Identification of elastic-plastic properties of metal materials by using the residual imprint of spherical indentation. Mater. Sci. Eng. A. **679**, 143–154 (2017). https://doi.org/10.1016/j.msea.2016.10.025

40. Meng, L., Breitkopf, P., Le Quilliec, G.: An insight into the identifiability of material properties by instrumented indentation test using manifold approach based on P-h curve and imprint shape. Int. J. Solids Struct. **106–107**, 13–26 (2017). https://doi.org/10.1016/j.ijsolstr.2016.12.002

41. Bolzon, G., Rivolta, B., Nykyforchyn, H., Zvirko, O.: Mechanical analysis at different scales of gas pipelines. Eng. Fail. Anal. **90**, 434–439 (2018). https://doi.org/10.1016/j.engfailanal.2018.04.008

42. Xia, W., Dehm, G., Brinckmann, S.: Insight into indentation-induced plastic flow in austenitic stainless steel. J. Mater. Sci. **55**, 9095–9108 (2020). https://doi.org/10.1007/s10853-020-04646-y

43. Hwang, Y., Marimuthu, K.P., Kim, N., Lee, C., Lee, H.: Extracting plastic properties from in-plane displacement data of spherical indentation imprint. Int. J. Mech. Sci. **197**, 106291 (2021). https://doi.org/10.1016/j.ijmecsci.2021.106291

44. Helmli, F.: Focus variation instruments. In: Leach, R. (ed.) Optical Measurement of Surface Topography, pp. 131–166. Springer, Berlin (2011)

45. Macdonald, D.A.: The application of focus variation microscopy for lithic use-wear quantification. J. Archaeol. Sci. **48**, 26–33 (2014). https://doi.org/10.1016/j.jas.2013.10.003

46. Kapłonek, W., Nadolny, K., Królczyk, G.M.: The use of focus-variation microscopy for the assessment of active surfaces of a new generation of coated abrasive tools. Meas. Sci. Rev. **16**, 42–53 (2016). https://doi.org/10.1515/msr-2016-0007

47. Newton, L., Senin, N., Gomez, C., Danzl, R., Helmli, F., Blunt, L., Leach, R.: Areal topography measurement of metal additive surfaces using focus variation microscopy. Addit. Manuf. **25**, 365–389 (2019). https://doi.org/10.1016/j.addma.2018.11.013

48. Yuan, L., Guo, T., Qiu, Z., Fu, X., Hu, X.: An analysis of the focus variation microscope and its application in the measurement of tool parameter. Int. J. Precis Eng. Manuf. **21**, 2249–2261 (2020). https://doi.org/10.1007/s12541-020-00419-4

49. Bolzon, G., Talassi, M.: Non-destructive integrity assessment of aging steel components. Int. J. Pres. Ves Pip. **198**, 104673 (2022). https://doi.org/10.1016/j.ijpvp.2022.104673

50. Seok, C., Koo, J.: Evaluation of material degradation of 1Cr-1Mo-0.25V steel by ball indentation and resistivity. J. Mater. Sci. **41**, 1081–1087 (2006). https://doi.org/10.1007/s10853-005-3644-6

51. Chen, X., Yan, J., Karlsson, A.M.: On the determination of residual stress and mechanical properties by indentation. Mater. Sci. Eng. A. **416**, 139–149 (2006). https://doi.org/10.1016/j.msea.2005.10.034

52. Ahles, A.A., Emery, J.D., Dunand, D.C.: Mechanical properties of meteoritic Fe–Ni alloys for in-situ extraterrestrial structures. Acta Astronaut. **189**, 465–475 (2021). https://doi.org/10.1016/j.actaastro.2021.09.001

53. Broitman, E.: Indentation hardness measurements at macro-, micro-, and nanoscale: A critical overview. Trib Lett. **65**(23), 1–18 (2016). https://doi.org/10.1007/s11249-016-0805-5

54. Bolzon, G., Bocciarelli, M., Chiarullo, E.J.: Mechanical characterisation of materials by microindentation and AFM scanning. In: Bhushan, B., Fuchs, H. (eds.) Applied Scanning Probe Methods XII Characterization, pp. 85–120. Springer, Heidelberg (2008). https://doi.org/10.1007/978-3-540-85039-7_5

55. EN ISO 6508:2005. Metallic materials—Rockwell hardness test: (2005)

56. ASTM E18–20, Standard test methods for Rockwell hardness of metallic materials: (2020)

57. Bolzon, G., Talassi, M.: Model reduction techniques in computational materials mechanics. In: Zavarise, G., Boso, D. (eds.) Bytes and Science, pp. 131–143. CIMNE, Barcelona (2012)

58. Bolzon, G.: Potentially automated mechanical characterization of metal components by means of hardness test complemented by non-contact 3D measurement. J. Phys.: Conf. Ser. **2293**, 012010 (2022). https://doi.org/10.1088/1742-6596/2293/1/012010

59. Schwab, R., Harter, A.: Extracting true stresses and strains from nominal stresses and strains in tensile testing. Strain. **57**, e12396 (2021). https://doi.org/10.1111/str.12396

60. https://www.alicona.com/en/products/infinitefocussl, last retrieved on 22/06/2023

61. Bolzon, G., Maier, G., Panico, M.: Material model calibration by indentation, imprint mapping and inverse analysis. Int. J. Solids Struct. **41**, 2957–2975 (2004). https://doi.org/10.1016/j.ijsolstr.2004.01.025

62. Matlab, R.: The Math Works Inc., Natick, MA (2021)

63. Ly, H.V., Tran, H.T.: Modeling and control of physical processes using proper orthogonal decomposition. Math. Comput. Model. **33**, 223–236 (2001). https://doi.org/10.1016/S0895-7177(00)00240-5